

Dynamics around supermassive black holes: Extreme-mass-ratio inspirals as Gravitational-wave Sources

BARAK ROM ¹, ITAI LINIAL ^{2,3}, KARAMVEER KAUR ^{4,1} AND RE'EM SARI ¹

¹*Racah Institute of Physics, The Hebrew University of Jerusalem, 9190401, Israel*

²*Department of Physics and Columbia Astrophysics Laboratory, Columbia University, New York, NY 10027, USA*

³*Institute for Advanced Study, 1 Einstein Drive, Princeton, NJ 08540, USA*

⁴*Technion - Israel Institute of Technology, Haifa, 3200002, Israel*

ABSTRACT

Supermassive black holes and their surrounding dense stellar environments nourish a variety of astrophysical phenomena. We focus on the distribution of stellar-mass black holes around the supermassive black hole and the consequent formation of extreme-mass-ratio inspirals (EMRIs). We derive a steady-state distribution, considering the effects of two-body scattering and gravitational-wave emission, and calculate the EMRI formation rate, eccentricity distribution, and EMRI-to-plunge ratio. Our model predicts: **(a)** a stronger segregation than previously estimated at the outskirts of the sphere of influence (at $\sim 0.01 - 2$ pc for a Milky Way-like galaxy); **(b)** an increased EMRI-to-plunge ratio, favoring EMRIs at galaxies where stellar-mass black holes are scarce; **(c)** a detection of about 2×10^3 resolvable EMRIs, with a signal-to-noise ratio above 20, along a 4 yr LISA mission time; and **(d)** a confusion noise, induced by a cosmological population of unresolved EMRIs, reducing the LISA sensitivity in the 1 – 5 mHz frequency range by up to a factor of ≈ 2 , relative to the instrumental noise.

Keywords: Galactic center (565), Stellar dynamics (1596), Supermassive black holes (1663), Stellar mass black holes(1611), Gravitational wave sources(677), Gravitational wave detectors(676)

1. INTRODUCTION

Supermassive black holes (SMBHs) and their surrounding nuclear stellar clusters (NSCs) reside at the centers of galaxies and cultivate a plethora of astrophysical phenomena: from quasars and active galactic nuclei (Schmidt 1963; Netzer 2015) to tidal disruption events (TDEs; Rees 1988; Gezari 2021) and quasiperiodic eruptions (QPEs; Miniutti et al. 2019; Arcodia et al. 2021). Furthermore, the dense stellar environment in galactic nuclei is a fertile ground for gravitational-wave (GW) sources, including merging stellar-mass black hole (sBH) binaries (Mapelli 2021; Arca Sedda et al. 2023), observable by the LIGO-Virgo-KAGRA collaboration, and mergers of sBHs with the SMBH, i.e., extreme-mass-ratio inspirals (EMRIs). The latter are expected to be primary GW sources for the space-based observa-

tory LISA (Amaro-Seoane et al. 2023), with an expected detection rate of a few to thousands of EMRIs per year (Gair et al. 2004; Mapelli et al. 2012; Babak et al. 2017; Bonetti & Sesana 2020; Pozzoli et al. 2023). The large span in the estimated detection rate is mostly due to the uncertainties regarding the SMBH mass function and the EMRI rate per galaxy, ranging between ~ 10 and 10^3 Gyr⁻¹ (Hils & Bender 1995; Sigurdsson & Rees 1997; Ivanov 2002; Hopman & Alexander 2005; Amaro-Seoane & Preto 2011; Merritt 2015; Aharon & Perets 2016; Bar-Or & Alexander 2016; Vázquez-Aceves et al. 2022; Broggi et al. 2022).

The EMRI rate per galaxy depends on the stellar dynamics in the NSC, which has been extensively studied for over half a century. Bahcall & Wolf (1976) derived a zero-flux steady-state solution for a single-mass population, under the assumptions of spatial spherical symmetry with isotropic velocities, where the dynamics are dominated by weak two-body scattering. In this case, the phase-space distribution is given by $f(E) \propto E^p$ with $p = 1/4$, and so the number density scales as $n(r) \propto r^{-\gamma}$,

with $\gamma = 3/2 + p = 7/4$ (hereafter, the BW profile). This solution satisfies a vanishing particle flux and a constant energy flux (Rom et al. 2023). In a following paper, Bahcall & Wolf (1977) generalized their calculation for multimass groups. Assuming that the most massive objects, with mass m_{\max} , are the most abundant, a zero-flux solution is satisfied when the massive group follows the single-mass BW profile, with $p_{\max} = 1/4$, while the lighter objects, with mass $m_i < m_{\max}$, obtain shallower profiles, $p_i/p_{\max} \approx m_i/m_{\max}$ (Bahcall & Wolf 1977; Linial & Sari 2022).

However, when considering realistic NSCs, the light stars typically occur in much greater numbers than heavier compact objects. This led Alexander & Hopman (2009) to derive the ‘‘strong mass segregation’’ solution (see, for example, Amaro-Seoane & Preto 2011; Aharon & Perets 2016; Amaro-Seoane 2018), which takes into account the drift of the massive objects toward the center of the cluster due to dynamical friction. The solution of Alexander & Hopman (2009) predicts that the light stars obtain the single-mass BW profile while the heavier objects follow a steeper profile, with $p = 5/4$, corresponding to a nonzero constant inward flux. This solution was generalized for a continuous mass function by Keshet et al. (2009).

Recently, Linial & Sari (2022) have derived a steady-state solution for a continuous mass function that takes into account the dominance of different mass groups in different energy bins. Thus, this solution provides a self-consistent zero-flux solution in all energy bins and for each mass group simultaneously.

The steady-state distributions of the sBHs and stars affect the formation rates of the center-of-galaxy associated transients, such as TDEs, QPEs, and EMRIs, mainly through the interplay between two-body scattering and GW emission (Alexander 2017; Amaro-Seoane et al. 2023). Qualitatively, two-body scattering leads to a diffusion in angular momentum, producing highly eccentric orbits that efficiently dissipate energy by GW emission (e.g., Hopman & Alexander 2005; Hopman 2009; Amaro-Seoane & Preto 2011; Aharon & Perets 2016; Sari & Fragione 2019; Linial & Sari 2023).

In this work, we apply the general solution of Linial & Sari (2022) to a simplified model of a two-mass NSC, including solar-mass stars and sBHs. We introduce modifications to the steady-state distributions due to GW emission and derive analytically the characteristics of the resulting EMRIs. In Section 2, we derive the spatial distribution of the sBHs. In Section 3, we calculate the EMRI rate per galaxy, their eccentricity distribution, and the EMRI-to-plunge ratio. In Section 4 we estimate the expected number of EMRIs that will be detected by

Table 1. Distances Glossary

Symbol	Eq.	Definition
R_h	1	Radius of influence of the SMBH.
R_s	5	Schwarzschild radius of the SMBH.
$r_{p,lc}(r)$	7	Effective loss-cone due to GW emission - the periapsis below which GW dominates, for a given semimajor axis r .
R_c	8	Distance differentiating plunge ($r \gtrsim R_c$) and EMRI ($r \lesssim R_c$) progenitors.
R_I	10	Characteristic distance below which sBHs are the dominant scatterers.
R_{II}	14	Characteristic distance replenished by sBHs initially at R_I , defined as $R_{II} = r_{p,lc}(R_I)$.
R_{GW}	16	Transition from scattering-dominated to GW-dominated dynamics for circular orbits, defined as $R_{GW} = r_{p,lc}(R_{GW})$.
R_t	18	Stellar tidal radius.

LISA and the residual GW background (GWB) from unresolved EMRIs. In Section 5 we compare our model with known results in the literature. Finally, we summarize our results in Section 6.

2. STEADY-STATE DISTRIBUTIONS IN NSCS

We study the distribution of stars and sBHs in the NSC that surrounds an SMBH of mass M_{BH} . We assume that the cluster consists of solar-mass stars, $m_{\star} = M_{\odot}$, and sBHs, with $m_{\bullet} = 10M_{\odot}$. Key scale radii are summarized in Table 1. We focus on the dynamics within the radius of influence R_h , where the SMBH dominates the gravitational potential. Using the $M \propto \sigma_h^{\beta}$ relation, where σ_h is the stellar velocity dispersion and $\beta = 4$ (Kormendy & Ho 2013), the radius of influence is given by

$$R_h = \frac{GM_{\text{BH}}}{\sigma_h^2} \simeq 2 \text{ pc} \left(\frac{M_{\text{BH}}}{M_{\text{MW}}} \right)^s, \quad (1)$$

where $s = 1 - 2/\beta = 1/2$. We normalize M_{BH} to the mass of Sgr A*, $M_{\text{MW}} = 4 \times 10^6 M_{\odot}$ (Ghez et al. 2008; Gillessen et al. 2009).

The steady-state distributions of stars and sBHs are determined by two-body scattering, which dominates at large distances from the SMBH, and dissipation due to GW emission, which takes over at the vicinity of the SMBH.

Two-body scattering introduces a characteristic timescale for the angular momentum of a given orbit

to change by order of itself:

$$\tau_{2B}^{(J)}(r, r_p) = \frac{3\sqrt{2}\pi(3-\gamma)}{32c_{7/4}\log\Lambda} \frac{P(r)}{N_{\bullet}(r)} \left(\frac{M_{\text{BH}}}{m_{\bullet}}\right)^2 \frac{r_p}{r}, \quad (2)$$

where r is the semimajor axis, r_p is the periapsis, $P(r)$ is the orbital period, $\log\Lambda$ is the Coulomb logarithm, with $\Lambda \approx M_{\text{BH}}/m_{\star}$ (typically $\log\Lambda \sim 10$), and $N_{\bullet}(r)$ is roughly the number of sBHs with semimajor axis between $r/2$ and r , defined as

$$N_{\bullet}(r) = 4\pi r^3 n_{\bullet}(r), \quad (3)$$

where $n_{\bullet}(r) \propto r^{-\gamma}$ is the sBH number density. The numerical prefactor in Eq. (2) is determined by the orbit-averaged diffusion coefficient (Merritt et al. 2010), with c_{γ} depending on the scatterer number density, for a BW profile $c_{7/4} = 1.35$ (Bortolas & Mapelli 2019). Note that in Eq. (2) we assume that the sBHs dominate the scattering, which is valid at distances of order $r/R_h \lesssim 10^{-2}$, as discussed below.

The GW characteristic energy-loss timescale, E/\dot{E} , for sBHs on highly eccentric orbits¹ is given by (Peters 1964):

$$\tau_{\text{GW}}^{(E)}(r, r_p) = \frac{96\sqrt{2}}{85} \frac{R_s}{c} \frac{M_{\text{BH}}}{m_{\bullet}} \left(\frac{r_p}{R_s}\right)^4 \sqrt{\frac{r}{r_p}}, \quad (4)$$

where R_s is the Schwarzschild radius of the SMBH, given by

$$R_s = \frac{2GM_{\text{BH}}}{c^2} \simeq 4 \times 10^{-7} \text{ pc} \left(\frac{M_{\text{BH}}}{M_{\text{MW}}}\right). \quad (5)$$

The transition between the scattering-dominated region and the GW-dominated one occurs when the two-body scattering timescale (Eq. 2) and the GW timescale (Eq. 4) are comparable (Hopman & Alexander 2005; Amaro-Seoane 2018; Sari & Fragione 2019)

$$\tau_{\text{GW}}^{(E)} = S \times \tau_{2B}^{(J)}, \quad (6)$$

where $S \simeq 1.36$, as determined by numerically solving the Fokker-Planck equation (see Kaur et al. 2024). Eq. (6) defines an effective loss-cone boundary in the (r, r_p) plane, given by

$$\begin{aligned} \frac{r_{p,\text{lc}}}{R_s} &= c_p \alpha^{2/5} \left(\frac{m_{\star}}{m_{\bullet}}\right)^{-1/5} \left(\frac{r}{R_h}\right)^{-1/2} \\ &\simeq 0.7 \left(\frac{r}{R_h}\right)^{-1/2}, \end{aligned} \quad (7)$$

¹ A GR correction to the GW timescale, Eq. (4), was introduced by Zwick et al. (2021). However, for a nonspinning SMBH, it yields an order unity correction to the formation rate (see Vázquez-Aceves et al. 2022) and therefore we neglect it here.

where $\alpha = 425\pi^2 / (2048\sqrt{2}c_{7/4}\log\Lambda) \simeq 0.11$ and $c_p = S^{2/5} = 1.13$, as defined in Kaur et al. (2024). Above this line, i.e., for $r_p > r_{p,\text{lc}}$, two-body scattering dominates the orbital evolution, leading to a random walk in r_p , while below it, the orbit shrinks and circularizes due to GW emission, as depicted in Fig. (1). In the derivation of Eq. (7), we assume that the sBHs follow a BW profile.

Although Eq. (7) was derived under the assumption that sBHs dominate the scattering, it remains valid in regions where the stars are the dominant scatterers. This is because the stars have a smaller cross section compared to the sBHs but they are more numerous. These two effects balance out when the BW profile of sBHs is normalized according to Linial & Sari (2022), as discussed below (see Eqs. 9 and 15).

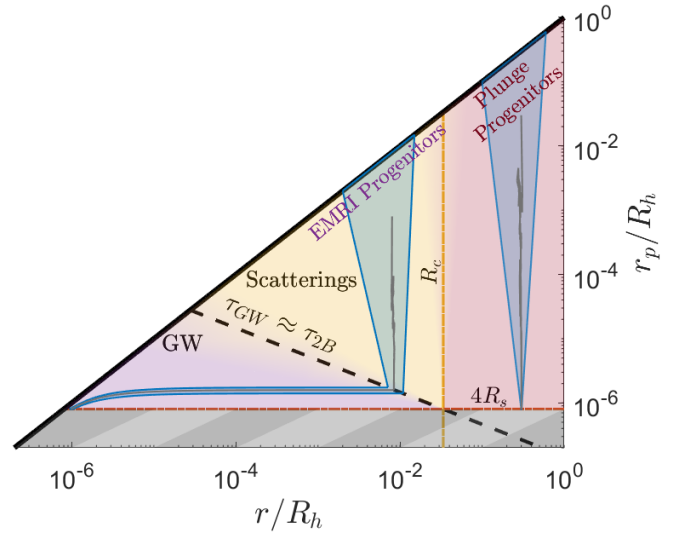


Figure 1. Orbital dynamics in the (r, r_p) phase space, where r is the semimajor axis and r_p is the periapsis. The dashed black line distinguishes between the two-body-scattering-dominated region and the GW-dominated one (Eq. 7); above it, the scattering leads to a diffusion dominantly in the r_p direction (as encapsulated by the shaded vertical blue funnel), while below it, GW emission efficiently shrinks and circularizes the orbit (along the horizontal shaded funnel). The red dashed-dotted line marks the mostly bound orbit, with $r_p = 4R_s$, and the yellow dashed-dotted line represents the critical semimajor axis R_c (Eq. 8), separating EMRI progenitors (with $r \lesssim R_c$) and plunge progenitors (with $r \gtrsim R_c$). The gray lines demonstrate examples of trajectories leading to an EMRI or a plunge, according to their initial semimajor axis.

The combined effect of diffusion of sBHs in angular momentum due to two-body scattering and circularization due to GW emission may lead either to a slowly evolving EMRI or to a rapid plunge, where the sBH reaches a periapsis smaller than the mostly bound orbit, $r_p = 4R_s$. The latter introduces a critical semimajor

axis: (Hopman & Alexander 2005)

$$\frac{R_c}{R_h} \simeq 0.03 \left(\frac{m_\star/m_\bullet}{0.1} \right)^{-2/5}, \quad (8)$$

which is given by Eq. (7) with $r_{p,\text{lc}}(R_c) = 4R_s$ (and see Fig. 1). Thus, direct plunges originate from orbits with $r \gtrsim R_c$, while orbits with $r \lesssim R_c$ lead to the formation of EMRIs, as they enter the GW-dominated region and circularize before plunging into the SMBH. Note that this dichotomy between the progenitors of EMRIs and plunges is less pronounced for $M_{\text{BH}} \lesssim 10^5 M_\odot$ (Qunbar & Stone 2023).

In the region where two-body scattering dominates the orbital evolution, the steady-state distributions of the sBHs and the stars satisfy a zero-flux solution (Bahcall & Wolf 1976; Linial & Sari 2022). Hence, at the outermost regions, up to R_h , the stars dominate the scattering and therefore settle into the BW profile and the sBHs number density follows a steeper profile, $n_\bullet(r) \propto r^{-3/2 - m_\bullet/(4m_\star)} = r^{-4}$, as they efficiently migrate inward, following the result of Linial & Sari (2022), who showed that $p_\bullet/p_\star \approx m_\bullet/m_\star$. Since the sBH density increases at smaller distances, at a certain distance, defined below as R_I , the sBHs become the dominant scatterers. Therefore, for $r < R_I$, the sBHs follow the BW profile while the stars obtain a shallower profile, with $p_\star = m_\star/(4m_\bullet)$, and so $n_\star(r) \propto r^{-3/2}$. Note that the number of stars is normalized such that the total mass of the stars within the radius of influence is roughly twice the SMBH's mass (Binney & Tremaine 1987; Merritt 2004), i.e., $N_\star(R_h) \approx 2M_{\text{BH}}/m_\star$, while the normalization of the sBH distribution ensures a continuous zero-flux solution (Linial & Sari 2022):

$$\frac{n_\bullet(R_I)}{n_\star(R_I)} = \left(\frac{m_\star}{m_\bullet} \right)^{3/2} \quad (9)$$

The transition between the star-dominated scattering region to sBH-dominated one, R_I , as defined implicitly by Eq. (9), is given by

$$\frac{R_I}{R_h} = f_\bullet^{4/5} \left(\frac{m_\star}{m_\bullet} \right)^{-6/5} \simeq 0.06 \left(\frac{f_\bullet}{10^{-3}} \right)^{4/5}, \quad (10)$$

where we define the sBH number fraction as

$$f_\bullet = \frac{N_\bullet(R_I)}{N_\star(R_h)}. \quad (11)$$

Namely, the total number of sBHs within the sphere of influence, which is dominated by their number around R_I , $N_\bullet(R_I)$, is a fraction f_\bullet of the number of stars within the sphere of influence, $N_\star(R_h) \approx 2M_{\text{BH}}/m_\star$.

Comparing R_c (Eq. 8) and R_I (Eq. 10) introduces a critical sBH number fraction,

$$f_\bullet^c \simeq 4.5 \times 10^{-4} \left(\frac{m_\bullet/m_\star}{10} \right), \quad (12)$$

such that $R_I > R_c$ for $f_\bullet > f_\bullet^c$ and vice versa. The critical number fraction f_\bullet^c distinguishes between two qualitatively different EMRI formation scenarios, as discussed in Section (3).

The GW-dominated region is characterized by a broken power law as well. At the immediate vicinity of the SMBH, up to a characteristic distance R_{II} , as defined below, the steady-state distribution is determined by the GW timescale (Eq. 4). Hence, considering circular orbits, $N_\bullet(r) \sim \tau_{\text{GW}}^{(E)} \propto r^4$. However, at greater distances, $r > R_{\text{II}}$, there is an effective replenishment of sBHs by two-body scattering, which leads to a shallower profile. The profile due to the replenishment of circular orbits can be determined by equating the two-body-scattering-induced flux, in the r_p -direction at a given semimajor axis \tilde{r} , and the GW flux, in the r -direction:

$$\frac{N_\bullet(r)}{\tau_{\text{GW}}^{(E)}(r)} = \frac{N_\bullet(\tilde{r})}{\tau_{2B}^{(J)}(\tilde{r}) \log \Lambda_0}, \quad (13)$$

where $\log \Lambda_0 = \log [r/r_{p,\text{lc}}(r)] \approx \log (R_c/R_s)$, is roughly the size of the relevant loss-cone and $r = r_{p,\text{lc}}(\tilde{r})$, as given by Eq. (7). In Eq. (13), we use the two-body timescale and GW timescale for nearly circular orbits, i.e., Eqs. (2) and (4) with $r \approx r_p$. Substituting the BW profile, $n_\bullet(\tilde{r}) \propto \tilde{r}^{-7/4}$, yields $N_\bullet(r) \propto r^2$. Note that the two-body scattering flux assumes an empty loss-cone dynamics (Lightman & Shapiro 1977), as further discussed in Section 3.

As mentioned above, R_{II} is the characteristic distance that is supplemented by the flux of sBHs with initial semimajor axis of $\sim \min \{R_I, R_c\}$, namely $R_{\text{II}} = r_{p,\text{lc}}(\min \{R_I, R_c\})$ or

$$\frac{R_{\text{II}}}{R_s} = 4 \times \max \left\{ 1, \left(\frac{f_\bullet^c}{f_\bullet} \right)^{2/5} \right\}. \quad (14)$$

Thus, the number density of sBHs is given by

$$n_\bullet(r) = \frac{1}{2\pi R_h^3} \frac{M_{\text{BH}}}{m_\star} \times \begin{cases} f_\bullet^{9/5} \left(\frac{m_\star}{m_\bullet} \right)^{-6/5} \left(\frac{r}{R_h} \right)^{-4} & R_I < r < R_h \\ \left(\frac{m_\star}{m_\bullet} \right)^{3/2} \left(\frac{r}{R_h} \right)^{-7/4} & R_{\text{GW}} < r < R_I \\ C_1 \left(\frac{m_\star}{m_\bullet} \right)^{8/5} \left(\frac{R_s}{R_h} \right)^{-3/2} \left(\frac{r}{R_s} \right)^{-1} & R_{\text{II}} < r < R_{\text{GW}} \\ C_2 f_\bullet^{4/5} \left(\frac{m_\star}{m_\bullet} \right)^{4/5} \left(\frac{R_s}{R_h} \right)^{-3/2} \frac{r}{R_s} & R_s \lesssim r < R_{\text{II}} \end{cases}, \quad (15)$$

where R_{GW} is determined such that the sBH distribution is continuous, qualitatively corresponding to the distance where $\tau_{\text{GW}}^{(E)}(r) \sim \tau_{2B}^{(J)}(r)$,

$$\begin{aligned} \frac{R_{\text{GW}}}{R_s} &= \left(\frac{\log \Lambda_0 \alpha^{1/5}}{c_p^2} \right)^{4/3} \left(\frac{m_\star}{m_\bullet} \right)^{-2/15} \left(\frac{R_s}{R_h} \right)^{-1/3} \\ &\approx 2 \times 10^3 \left(\frac{M_{\text{BH}}}{M_{\text{MW}}} \right)^{-1/6}, \end{aligned} \quad (16)$$

and the numerical order unity coefficients C_1 and C_2 are given by

$$\begin{aligned} C_1 &= \frac{c_p^2}{\alpha^{1/5} \log \Lambda_0} \approx 0.2, \\ C_2 &= \frac{\min\{1, f_\bullet^c/f_\bullet\}^{4/5}}{\alpha \log \Lambda_0} \\ &\approx 0.9 \min\{1, f_\bullet^c/f_\bullet\}^{4/5}, \end{aligned} \quad (17)$$

where we have substituted $\log \Lambda = \log \Lambda_0 = 10$.

For completeness, we present the corresponding distribution of the stars, from R_h to the tidal radius, where the SMBH tidal force is comparable to the star's self-gravity

$$\frac{R_t}{R_s} \approx \frac{R_\star}{R_s} \left(\frac{M_{\text{BH}}}{m_\star} \right)^{1/3} \simeq 9 \left(\frac{M_{\text{BH}}}{M_{\text{MW}}} \right)^{-2/3}, \quad (18)$$

where $R_\star = R_\odot$ is the radius of the star. However, unlike the sBH distribution, collisions are expected to significantly modify the star distribution (Sari & Fragione 2019; Rose et al. 2023; Balberg & Yassur 2023), hence we present only a qualitative analysis and leave a detailed calculation for a future work.

As mentioned above, at the outer parts of the NSC, where two-body scatterings dominate the orbital evolution, the stars distribution can be described by a broken power law, with $n_\star(r \geq R_I) \propto r^{-7/4}$ and $n_\star(r < R_I) \propto r^{-3/2}$. Considering only two-body scattering and GW emission, the stars qualitatively follow the flatter profile, $n_\star(r) \propto r^{-3/2}$, all the way² to $r \sim \max\{R_{\text{II}}, R_t\}$. Therefore, the number density of the stars, assuming $R_t > R_{\text{II}}$ (as depicted in Fig. 2), is roughly

$$\begin{aligned} n_\star(r) &\sim \frac{1}{2\pi R_h^3} \frac{M_{\text{BH}}}{m_\star} \\ &\times \begin{cases} \left(\frac{r}{R_h} \right)^{-7/4} & R_I < r < R_h \\ f_\bullet^{-1/5} \left(\frac{m_\star}{m_\bullet} \right)^{3/10} \left(\frac{r}{R_h} \right)^{-3/2} & R_t < r < R_I \end{cases}. \end{aligned} \quad (19)$$

² The stars at $r \lesssim R_{\text{GW}}$ are populated by two-body scattering replenishment via highly eccentric orbits. However, in practice, they follow almost the same power law, as it changes from $p_\star = m_\star/4m_\bullet$ to $p_\star = -m_\star/2m_\bullet$. Therefore, we neglect this transition and assume a constant $p_\star \approx 0$ at this region.

If $R_{\text{II}} > R_t$, which corresponds to $f_\bullet \lesssim 10^{-4}$, the replenishment of self-scattered stars would dominate the feeding rate of stars to the orbits below R_{II} and would therefore follow $n_\star \propto r^{-1}$, equivalently to the sBH distribution for $R_{\text{II}} < r < R_{\text{GW}}$.

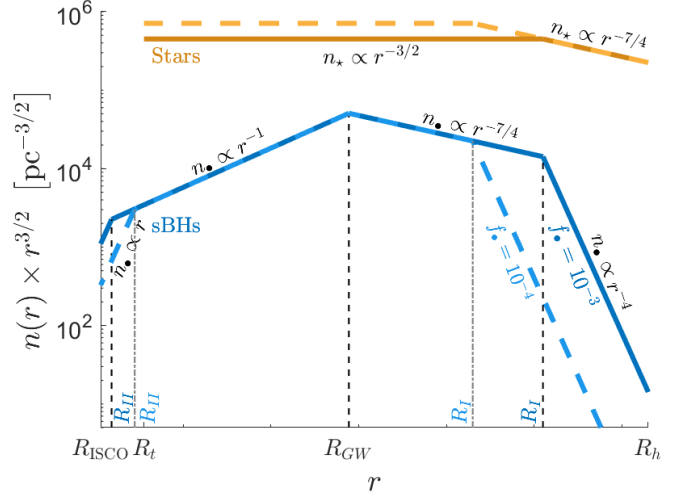


Figure 2. Steady-state distributions of the sBHs (blue lines) and the stars (yellow lines), as given by Eqs. (15) and (19). We consider a SMBH with $M_{\text{BH}} = 4 \times 10^6 M_\odot$ and sBH number fractions $f_\bullet = 10^{-3}$ (solid lines) and $f_\bullet = 10^{-4}$ (dashed lines), as defined in Eq. (11). We plot $n(r) \times r^{3/2}$, which corresponds to the commonly used phase-space density, $f(E)$. The star distribution extends from R_h to the tidal radius, R_t (Eq. 18), while the sBHs can reach $R_{\text{ISCO}} = 3R_s$.

In Fig. (2), we present the density distributions of the stars and sBHs (Eqs. 15 and 19), respectively. Note that the intermediate region of the sBH distribution, $n_\bullet(R_{\text{II}} < r < R_I)$, and the outer part of the star distribution, $n_\star(R_I < r < R_h)$, are universal, in the sense that their normalization does not depend on the sBH number fraction f_\bullet . We demonstrate that in Fig. (2), which depicts the distributions for $f_\bullet = 10^{-3}$ (solid lines) and $f_\bullet = 10^{-4}$ (dashed lines).

Our analysis assumes that the NSC reaches a steady state, which is valid for clusters surrounding SMBHs with masses $M_{\text{BH}} \lesssim 10^7 M_\odot$, for which the relaxation time is shorter than the Hubble time (Binney & Tremaine 1987; Bar-Or et al. 2013).

3. EMRI CHARACTERISTICS: FORMATION RATE AND ECCENTRICITY DISTRIBUTION

In a given galaxy, the instantaneous distribution of sBHs is described by Eq. (15), ensuring that the flux induced by GW emission aligns with the corresponding two-body scattering flux, which sets the rate at which sBHs enter the GW-dominated region (see Eq. 13). Consequently, the EMRI formation rate is given by

(Hopman & Alexander 2005):

$$\begin{aligned} \Gamma_{\text{EMRI}} &= \int_{R_{\text{GW}}}^{R_c} dr \frac{4\pi r^2 n_{\bullet}(r)}{\tau_{2B}^{(J)}(r) \log \Lambda_0} \\ &\approx 260 \left(\frac{M_{\text{BH}}}{M_{\text{MW}}} \right)^{-1/4} y_E(f_{\bullet}) \text{ Gyr}^{-1}, \end{aligned} \quad (20)$$

$$\text{with } y_E(f_{\bullet}) \approx \begin{cases} 1 & f_{\bullet} > f_{\bullet}^c \\ 850 f_{\bullet}^{4/5} & f_{\bullet} < f_{\bullet}^c \end{cases}.$$

Note that, generally, the $\log \Lambda_0$ term introduces a logarithmic dependence on the semimajor axis, which we simplify by taking it as a constant. We assume $\log \Lambda_0 = 10$, which roughly corresponds to its value at $\min\{R_I, R_c\}$, where most of the EMRIs are originated from.

The EMRI formation rate is dominated by the flux of sBHs from $\min\{R_I, R_c\}$, since $\Gamma_{\text{EMRI}} \propto r$, for $r < R_I$ and $\Gamma_{\text{EMRI}} \propto r^{-5/4}$, for $r > R_I$. Moreover, the value of the maximal EMRI formation rate, achieved for $f_{\bullet} > f_{\bullet}^c$, does not depend on f_{\bullet} .

Direct plunges - namely, sBHs with semimajor axis $r \gtrsim R_c$ that may reach $r_p \lesssim 4R_s$ by two-body scattering, before circularizing due to GW emission - occur at a rate

$$\begin{aligned} \Gamma_{\text{Plunge}} &= \int_{R_c}^{R_h} dr \frac{4\pi r^2 n_{\bullet}(r)}{\tau_{2B}^{(J)}(r) \log \Lambda_0} \\ &\approx 210 \left(\frac{M_{\text{BH}}}{M_{\text{MW}}} \right)^{-1/4} y_P(f_{\bullet}) \text{ Gyr}^{-1}, \end{aligned} \quad (21)$$

$$\text{where } y_P(f_{\bullet}) \approx \begin{cases} 1000 f_{\bullet}^{4/5} & f_{\bullet} > f_{\bullet}^c \\ (f_{\bullet}/f_{\bullet}^c)^{9/5} & f_{\bullet} < f_{\bullet}^c \end{cases}.$$

In Table (2), we present the EMRI and plunge formation rates for different values of f_{\bullet} . Note that the formation rates, both of EMRIs and plunges, are proportional to the orbital period at the radius of influence, $\Gamma_{\text{EMRI,Plunge}} \propto 1/P(R_h) \propto M_{\text{BH}}^{3/\beta-1}$, as previously derived by Hopman & Alexander (2005). Additionally, we assume $R_{\text{GW}} \ll R_I, R_c \ll R_h$, and therefore neglect the contributions from R_{GW} and R_h in Eqs. (20) and (21), respectively.

The above calculation assumes an empty loss-cone dynamics (Lightman & Shapiro 1977), which is valid for the relevant SMBH masses. A transition to a full loss-cone region, where $P(r)/\tau_{2B}^{(J)}(r, r_{p,\text{lc}}(r)) \gg \log \Lambda_0$ (Vasiliev & Merritt 2013), corresponds to $M_{\text{BH}} \ll 10^4 M_{\odot} (f_{\bullet}/10^{-3})^{2/3}$ and therefore is not considered here.

In Fig. (3) we present the EMRI-to-plunge ratio, as given in Eqs. (20) and (21). Considering the two limiting cases, if the sBHs are scarce,

$$\left. \frac{\Gamma_{\text{EMRI}}}{\Gamma_{\text{Plunge}}} \right|_{f_{\bullet} \ll f_{\bullet}^c} \approx 100 \left(\frac{10^{-5}}{f_{\bullet}} \right). \quad (22)$$

f_{\bullet}	$\Gamma_{\text{EMRI}} [\text{Gyr}^{-1}]$	$\Gamma_{\text{Plunge}} [\text{Gyr}^{-1}]$
10^{-2}	260	5000
10^{-3}	260	600
10^{-4}	130	15
10^{-5}	20	0.22

Table 2. Formation rates of EMRIs (Eq. 20) and plunges (Eq. 21) for different values of the sBHs number fraction f_{\bullet} , assuming an SMBH with $M_{\text{BH}} = 4 \times 10^6 M_{\odot}$ and a population of sBHs with mass $m_{\bullet} = 10 M_{\odot}$.

while if they are abundant,

$$\left. \frac{\Gamma_{\text{EMRI}}}{\Gamma_{\text{Plunge}}} \right|_{f_{\bullet} \gg f_{\bullet}^c} \approx 0.05 \left(\frac{10^{-2}}{f_{\bullet}} \right)^{4/5}. \quad (23)$$

For the full expressions and the dependence on the sBH mass, see Appendix A.

Our estimated EMRI formation rate for a Milky Way-like galaxy is comparable to previous results in the literature (e.g., Hopman & Alexander 2006; Amaro-Seoane & Preto 2011; Merritt 2015; Aharon & Perets 2016; Vázquez-Aceves et al. 2022; Broggi et al. 2022). However, we predict fewer plunges, compared to earlier studies, since in our model the sBHs are concentrated around $R_I \ll R_h$ rather than around R_h , as in the single-power-law models (e.g., Bar-Or & Alexander 2016). Notably, for a low sBH number fraction, $f_{\bullet} \lesssim 5 \times 10^{-3}$, the EMRI rate surpasses the plunge rate. see Section 5 for further discussion.

Finally, we note that EMRIs and plunges may originate from sBH binary disruptions (Hills 1988) as well. The contribution of such a scenario depends linearly on the sBH binary fraction and tends to increase more prominently the EMRI formation rate for a significantly large binary fraction (see Sari & Fragione 2019, for further details). We ignore this effect here.

3.1. EMRI Eccentricity Distribution

The eccentricity evolution of the sBH orbits at the GW-dominated region, from an initial periapsis $r_{p,i}$ with $e_i \approx 1$ up to the mostly bound orbit, can be evaluated using Peters (1964), such that the eccentricity e satisfies

$$g(e) = \frac{4R_s}{r_{p,i}} = \left(\frac{r_i}{R_c} \right)^{-1/2}, \quad (24)$$

where

$$g(e) = \frac{2e^{12/19}}{(1+e)} \left(\frac{304 + 121e^2}{425} \right)^{870/2299}. \quad (25)$$

Note that in the second equality in Eq. (24), we assume that $r_{p,i}$ is along the loss-cone boundary, hence it can be

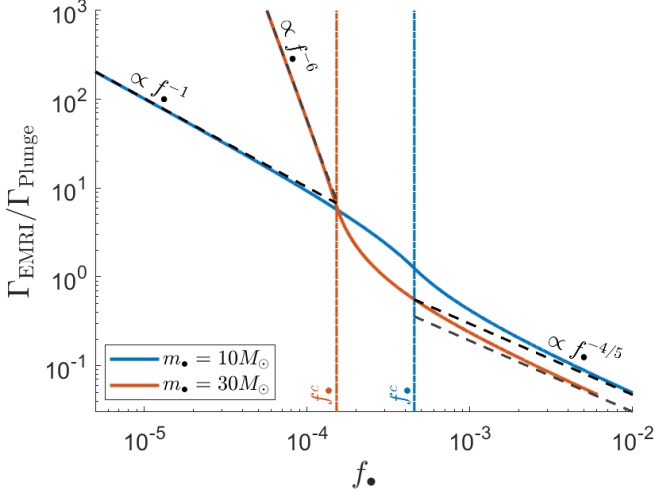


Figure 3. EMRI-to-plunge ratio as a function of the sBH number fraction, assuming sBHs of mass $m_{\bullet} = 10M_{\odot}$ (blue line) and $m_{\bullet} = 30M_{\odot}$ (red line), as calculated from Eqs. (20) and (21). The dashed-dotted lines mark the critical number density, f_{\bullet}^c (Eq. 12), for each sBH mass, with respective colors, and the dashed lines present the ratio in the limiting cases of scarce ($f_{\bullet} \ll f_{\bullet}^c$) and abundant ($f_{\bullet} \gg f_{\bullet}^c$) sBH population (Eqs. 22 and 23), respectively.

related to a semimajor axis r_i using Eq. (7), together with the definition of R_c (Eq. 8).

Thus, the minimal eccentricity is given by $g(e_{\min}) \simeq \frac{4R_s}{R_{\text{GW}}}$, or

$$e_{\min} \approx 10^{-5} \left(\frac{M_{\text{BH}}}{M_{\text{MW}}} \right)^{19/72}, \quad (26)$$

where we used $g(e \ll 1) \propto e^{12/19}$. On the other hand, the maximal eccentricity stems from sBHs with $r_i \approx R_c$, and therefore

$$(1 - e_{\max}) \approx \frac{4R_s}{R_c} \approx 10^{-5} \left(\frac{M_{\text{BH}}}{M_{\text{MW}}} \right)^{1/2}. \quad (27)$$

The eccentricity distribution depends on the number fraction of the sBHs f_{\bullet} . If $f_{\bullet} > f_{\bullet}^c$, i.e., $R_I > R_c$, all the EMRI progenitors initially follow a BW profile, leading to a two-body-scattering-induced flux $\mathcal{F}_{2B} \propto \Gamma_{\text{EMRI}} \propto r_i$ (as evident from Eq. 20) and, hence, using Eq. (24):

$$p(e)|_{f_{\bullet} \geq f_{\bullet}^c} = 2g(e)g'(e), \quad (28)$$

as derived by Linial & Sari (2023) in the context of stellar EMRIs. This distribution peaks at $e \simeq 0.08$, and scales as $p(e \ll 1) \propto e^{5/19}$.

In the second case, where $f_{\bullet} < f_{\bullet}^c$, there is a characteristic eccentricity, e_I , given by the implicit relation

$$g(e_I) \approx \frac{4R_s}{R_{\text{II}}}, \quad (29)$$

yielding, for example, $e_I \approx 0.2$ or $e_I \approx 0.04$, for $f_{\bullet} = 10^{-4}$ and $f_{\bullet} = 10^{-5}$, respectively. For $e < e_I$ we get

as before $p(e) \propto g(e)g'(e)$, while the EMRIs with $e > e_I$ originate from $r_i > R_I$, and hence follow a different two-body-scattering-induced flux, $\tilde{\mathcal{F}}_{2B} \propto r_i^{-5/4}$, which leads to $p(e) \propto g(e)^{-7/2}g'(e)$. Taking into account the probability distribution normalization, we get

$$p(e)|_{f_{\bullet} < f_{\bullet}^c} \simeq \frac{10g'(e)g(e)}{9g(e_I)^{-5/2} - 4} \times \begin{cases} g(e_I)^{-7/2} & e_{\min} \leq e \leq e_I \\ g(e)^{-9/2} & e_I < e \leq e_{\max} \end{cases}, \quad (30)$$

which reproduces Eq. (28) in the limit $e_I \rightarrow 1$. Additionally, the distribution scales as $p(e \ll 1) \propto e^{5/19}$, while $p(e \gtrsim e_I) \propto e^{-49/19}$. The eccentricity distributions, Eqs. (28) and (30), are presented in Fig. (4).

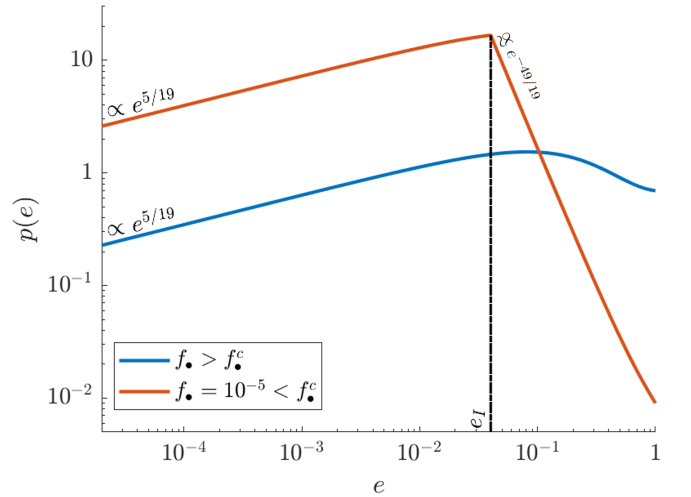


Figure 4. EMRI eccentricity probability density function at the mostly bound orbit. The blue line corresponds to the case where the sBH number fraction is larger than the critical value, $f_{\bullet} \geq f_{\bullet}^c$, where the distribution is independent of the specific value of f_{\bullet} and peaks at $e \simeq 0.08$. The red line exhibits an example of the complementary case, $f_{\bullet} = 10^{-5} < f_{\bullet}^c$, where the distribution peaks at $e_I \simeq 0.04$ (as given by Eq. 29) and falls steeply, as $p(e \gtrsim e_I) \propto e^{-49/19}$. In both cases, the distributions satisfy $p(e \ll 1) \propto e^{5/19}$.

4. EMRIS SIGNATURE AS GW SOURCES

Motivated by the tendency toward low eccentricities in the vicinity of the SMBH, as evident from Fig. (4), we focus on EMRIs where the sBH follows an adiabatic, quai-circular inspiral - namely it slowly descends from one circular orbit to another (for further details, see Appendix B). In this case, the GWs are emitted predominantly at twice the orbital frequency:

$$f = \frac{1}{\pi} \sqrt{\frac{GM_{\text{BH}}}{r^3}}. \quad (31)$$

The inclination-averaged characteristic strain of the GWs is given by (Finn & Thorne 2000):

$$h_c = \varepsilon_h \frac{8}{\sqrt{5}} (\pi f_{\text{obs}})^{2/3} \frac{(GM_{\text{obs}})^{5/3}}{c^4 d_L(z)} \sqrt{f_{\text{obs}} T_i^{\text{obs}}}, \quad (32)$$

where $\mathcal{M} = m_{\bullet}^{3/5} M_{\text{BH}}^{2/5}$ is the chirp mass, $M_{\text{obs}} = \mathcal{M}(1+z)$ is the observed (redshifted) chirp mass, $f_{\text{obs}} = f/(1+z)$ is the observed GW frequency, ε_h is the general relativity (GR) correction term (see Appendix B), and $d_L(z)$ is the luminosity distance (see Appendix C). The characteristic strain increases as the square root of the number of orbits the sBH undergoes at the frequency $\sim f_{\text{obs}}$, therefore

$$T_i^{\text{obs}} = \min \left\{ T_{\text{LISA}}, \frac{f_{\text{obs}}}{\dot{f}_{\text{obs}}} \right\}, \quad (33)$$

where $T_{\text{LISA}} = 4$ yr is the LISA mission time and

$$\frac{f_{\text{obs}}}{\dot{f}_{\text{obs}}} = \varepsilon_f \frac{5}{96} (\pi f_{\text{obs}})^{-8/3} \left(\frac{GM_{\text{obs}}}{c^3} \right)^{-5/3}, \quad (34)$$

where the dot corresponds to a derivative with respect to time in the detector frame and ε_f is the GR correction (see Appendix B). Qualitatively, T_i^{obs} separates between static, monochromatic sources ($f_{\text{obs}}/\dot{f}_{\text{obs}} > T_{\text{LISA}}$) and evolving sources ($f_{\text{obs}}/\dot{f}_{\text{obs}} < T_{\text{LISA}}$).

The number of sources, per frequency, SMBH mass, and redshift, is given by:

$$\begin{aligned} \mathcal{N} &= \frac{dN}{d(\log f_{\text{obs}}) d(\log M_{\text{obs}}) dz} \\ &= \frac{2}{3} N_{\bullet} \frac{T_{\text{LISA}}}{T_i^{\text{obs}}} \frac{d\rho_M}{d(\log M_{\text{obs}})} \frac{dV_c}{dz}, \end{aligned} \quad (35)$$

where $N_{\bullet}(M, f)$ is the sBH number in a given galaxy with orbital frequency $f/2$ (as given by Eqs. 3, 15, and 31), $M_{\text{obs}} = M_{\text{BH}}(1+z)$ is the observed SMBH mass, V_c is the comoving volume (see Appendix C), and the SMBH mass function is given by (Babak et al. 2017):

$$\frac{d\rho_M}{d(\log M_{\text{obs}})} = \rho_0 \left(\frac{M_{\text{BH}}}{M_{\text{MW}}} \right)^{-\zeta}, \quad (36)$$

with $\rho_0 = 0.005 \text{ Mpc}^{-3}$ and $\zeta = 0.3$. Note that in Eq. (35), the factor of $T_{\text{LISA}}/T_i^{\text{obs}}$ accounts for evolving sources that sweep a range of frequencies and the 2/3 prefactor stems from taking the derivative with respect to the frequency rather than the semimajor axis.

For evolving sources, $N_{\bullet} T_{\text{LISA}}/T_i \sim \Gamma_{\text{EMRI}} \times T_{\text{LISA}}$ - namely, the EMRI formation rate times the LISA mission time. For steady sources, the probability of having a source at a given galaxy corresponds to the number of sBHs with the relevant semimajor axis.

The total number of sources, per logarithmic frequency bin, with characteristic strain larger than h_c , is given by integrating Eq. (35) with respect to M_{obs} and z , which is related to h_c by Eq. (32).

We present in Fig. (5) the expected number of sources, assuming an sBH number fraction $f_{\bullet} = 10^{-3}$, along with the LISA sensitivity curve, $h_{c,\text{LISA}}$ (as given by Robson et al. 2019). In Fig. (6), we present a realization of our predicted sources distribution (Eq. 35), where each black line represents an EMRI. Thus, for example, we expect that during the LISA mission time, roughly one EMRI will be observed, per logarithmic frequency bin, with characteristic strain greater than the $dN/d(\log f_{\text{obs}}) = 1$ line in Figs. (5) and (6).

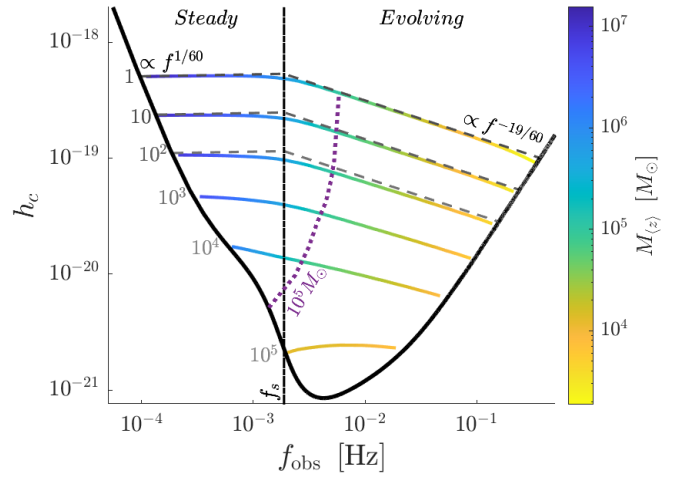


Figure 5. Characteristic strain of EMRIs as a function of the observed frequency. The black line is the LISA sensitivity curve (Robson et al. 2019) and the colored lines present contours of the observed sources numbers, between 1 and 10^5 , in a logarithmic frequency bin. The dashed lines present an analytical estimation at $z \ll 1$ (Eq. 40), scaling as $f^{1/60}$ at low frequencies and $f^{-19/60}$ at high frequencies. The color bar presents the source-frame SMBH mass that corresponds to the average redshift of the observed sources. The purple dotted line depicts the average SMBH mass $M_{(z)} = 10^5 M_{\odot}$.

In addition, we estimate the redshift expected value, $\langle z \rangle$, and its corresponding source-frame SMBH mass, $M_{(z)}$, at a given characteristic strain and observed frequency. We present the values of $M_{(z)}$ and $\langle z \rangle$ along the contours using color bars in Figs. (5) and (6), respectively. In Fig. (5), we present with a purple dotted line the contour of $M_{(z)} = 10^5 M_{\odot}$; below it, lighter SMBHs dominate the distribution, where the SMBH mass function and the $M_{\text{BH}} - \sigma_h$ relation are less constrained.

4.1. Analytical estimation of the observed source distribution

We can integrate the source distribution (Eq. 35), analytically by: (a) considering the local Universe, i.e., sources at $z \ll 1$, where the geometry is roughly flat; and (b) approximating the GR corrections as an effective numerical prefactor ε (as discussed in Section B).

Under these assumptions, substituting Eqs. (31) and (32) yields

$$\frac{dN}{d \log f} \Big|_{h_c} = \frac{4096\pi^3 G^5 m_\bullet^3 f^{7/2} T_{\text{LISA}} \rho_0 \varepsilon^3}{45\sqrt{5} c^{12} h_c^2} \times \int N_\bullet M_{\text{BH}}^{1-\zeta} T_i^{1/2} dM_{\text{BH}}. \quad (37)$$

The number of sources at each frequency bin is dominated by the SMBH with mass

$$M_{\text{max}} \approx 0.8 M_{\text{MW}} \left(\frac{1 \text{mHz}}{f} \right). \quad (38)$$

This can be understood as the SMBH for which the orbital frequency at its ISCO corresponds to the observed GW frequency, reduced by a numerical prefactor that encapsulates the shortened merger time from the ISCO (Ori & Thorne 2000; Buonanno & Damour 2000; Finn & Thorne 2000). As discussed in Appendix B, this prefactor, which we take as 0.8 in Eq. (38), ranges between ≈ 0.65 for evolving sources (at high frequencies, $f \gtrsim f_s$, as defined in Eq. 39), to ≈ 1 for steady sources (at low frequencies, $f \lesssim f_s$).

We further introduce a characteristic frequency, f_s , for which the merger time from the SMBH's ISCO is roughly the LISA mission time:

$$f_s \approx \frac{1}{2\pi} \sqrt{\frac{5c^3}{4Gm_\bullet T_{\text{LISA}}}} \approx 2 \text{mHz}, \quad (39)$$

Thus, at low frequencies, $f \lesssim f_s$, nearly steady, monochromatic EMRIs are the dominant sources, while at higher frequencies, $f \gtrsim f_s$, evolving sources, which sweep across a significant portion of the LISA band, become more prominent.

Finally, we get from Eq. (37), using Eqs. (15) and (33), the characteristic strain as a function of the observed frequency, for a given number of sources:

$$h_c \approx 5 \times 10^{-19} \left(\frac{f}{f_s} \right)^\delta \left(\frac{dN}{d \log f} \right)^{-1/3} \times \left(\frac{f_\bullet}{f_\bullet^c} \right)^{4/15} \frac{\xi(\min\{f_\bullet, f_\bullet^c\})}{\xi(f_\bullet^c)}. \quad (40)$$

For steady sources ($f \lesssim f_s$), $\delta = 1/60$ and $\xi(x) \simeq (1 - 17x^{47/100})^{1/3}$. For evolving sources ($f \gtrsim f_s$), $\delta = -19/60$ and $\xi(x) \simeq (1 - 5x^{27/100})^{1/3}$.

The analytical estimation agrees with the full numerical results at relatively large characteristic strains, $h_c \gtrsim 10^{-19}$, as presented in Fig (5), corresponding to nearby sources, and deviates when considering cosmological distances, which contribute to the lower values of h_c .

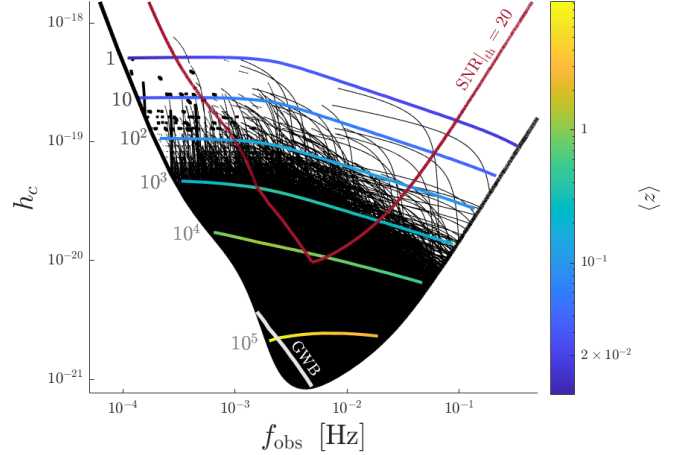


Figure 6. A realization of the observed EMRIs; each black line represents an EMRI, chosen according to the distribution given in Eq. (35), assuming an observation time $T_{\text{LISA}} = 4$ yr. As in Figure 5, the black thick line is the LISA sensitivity curve and the colored lines present contours of the observed sources numbers. The color bar presents the average redshift of the observed sources. The white line corresponds to the GWB (Eq. 41), assuming a limit of one source per 4 frequency bins, $\delta f = 1/T_{\text{LISA}}$. Roughly 2×10^3 resolvable sources lie above the red line, which depicts the $\text{SNR}|_{\text{th}} = 20$ threshold.

4.2. GW Background

In addition to the resolvable sources, with signal-to-noise ratio (SNR) greater than a given detectability threshold, $\text{SNR}|_{\text{th}}$, there is an accumulation of a stochastic GWB, induced by a population of unresolved sources. This effectively produces a background noise, a so-called confusion noise, which may decrease LISA's sensitivity, if it exceeds the intrinsic instrumental noise - as in the case of the galactic white dwarf binaries (Nelemans et al. 2001; Timpano et al. 2006; Ruiter et al. 2010; Nissanke et al. 2012; Cornish & Robson 2017).

The noise introduced by the EMRI GWB can be estimated as the characteristic strain for which there is one source per few frequency bins, $a \times \delta f$, with $\delta f = 1/T_{\text{LISA}}$. We take $a = 3$ as an effective parameter corresponding to the signal smearing, due to LISA's motion, as well as the limitations of the data analysis procedure (Hughes 2002; Barack & Cutler 2004; Tim-

pano et al. 2006). A numerical fit to the GWB yields

$$h_{c,\text{GWB}} \simeq 2.1 \times 10^{-21} \left(\frac{f}{2.5 \text{ mHz}} \right)^{-1.26}. \quad (41)$$

In Fig. (6), we present the GWB in the range $\sim 1 - 5$ mHz, where it surpasses the LISA instrumental noise, by up to a factor of ≈ 2 around 2.5 mHz.

Given the EMRI GWB, we can estimate the number of resolvable sources. The SNR of a source, averaged over sky location, inclination, and polarization, is given by (Robson et al. 2019):

$$\text{SNR}^2 = \frac{16}{5} \int d \log f_{\text{obs}} \left(\frac{h_c}{h_{c,\text{noise}}} \right)^2, \quad (42)$$

where $h_{c,\text{noise}} = \max\{h_{c,\text{LISA}}, h_{c,\text{GWB}}\}$. We estimate the number of resolvable sources by averaging the number of sources with $\text{SNR} \geq \text{SNR}|_{\text{th}}$, calculated using Eq. (42), over 10 different realizations of our source distribution (Eq. 35); one of these realizations is presented in Fig. (6).

Considering a 4 yr mission time, we expect about 2×10^3 resolvable sources, with SNR above $\text{SNR}|_{\text{th}} = 20$. A lower SNR threshold, e.g., $\text{SNR}|_{\text{th}} = 8$, increases the number of resolvable sources by a factor of ≈ 5 . Note that other sources and formation channels, e.g., EMRIs from SMBH binaries (Naoz & Haiman 2023), may induce a stronger GWB, which will reduce the number of resolvable sources estimated here.

5. COMPARISON WITH PREVIOUS WORKS

In this work, we present several modifications to the widely used steady-state distributions in NSCs and the EMRI formation mechanism. The following section summarizes the main differences between our analysis and previous results in the literature.

On the outskirts of the sphere of influence, external to R_I , where strong segregation occurs, we apply the result of Linial & Sari (2022) for the steady-state distribution. Therefore, our sBH density profile, $n_{\bullet} \propto r^{-4}$, is steeper than the ‘‘strong mass segregation’’ profile of Alexander & Hopman (2009). Moreover, the distributions of the sBHs and the stars (Eqs. 15 and 19) ensure a global zero-flux solution and thus a smooth transition between the star-dominated region, at $r \gtrsim R_I$, and the sBH-dominated one, at $r \lesssim R_I$ (for further details, see Linial & Sari 2022).

A main outcome of our model is the broken-power-law density distribution of sBHs (Eq. 15), rather than a single power law, where the number density’s exponent is $\gamma = 7/4$, for a BW profile, or $\gamma \approx 2$, for a strongly segregated cusp. In both of the latter distributions, the

majority of the sBHs are around $r \sim R_h$. Since EMRIs originate from $r \sim R_c \ll R_h$ (see Eq. 8), these models predict that plunges are more common than EMRIs, roughly by a factor of $R_h/R_c \sim 30$ (Alexander 2017). However, in our steady-state distribution, the sBHs are concentrated at $r \sim R_I$ (Eq. 10), leading to a reduced rate of plunges, compared to the single-power-law models. Furthermore, we predict that EMRIs become more common than plunges if $R_I \leq R_c$, i.e., $f_{\bullet} \leq f_{\bullet}^c$.

Considering the eccentricity distribution, we find that at the mostly bound orbit, the EMRI eccentricity follows a narrow distribution, peaking at small residual eccentricity, $e \lesssim 0.1$, which is compatible with previous estimates (e.g., Babak et al. 2017).

Regarding the eccentricity evolution throughout the merger, we adopt a simplified approach. While other studies (e.g., Bonetti & Sesana 2020; Pozzoli et al. 2023) account for the broadband GW emission along eccentric orbits, we calculate the GW strain assuming circular orbits. This is motivated by the typically low eccentricities at the vicinity of the SMBH, as discussed above. Moreover, emission from tightly bound, nearly circular orbits dominates over that from eccentric orbits at the same frequency (Peters & Mathews 1963). Thus, our method captures the dominant GW signal, though it neglects the extended, lower-frequency tail associated with the circularization of eccentric orbits during the merger.

Previous estimations of the number of sources detectable by LISA span 3 orders of magnitude, from a few to thousands of EMRIs per year (Barack & Cutler 2004; Gair et al. 2004; Mapelli et al. 2012; Babak et al. 2017; Bonetti & Sesana 2020; Pozzoli et al. 2023). Babak et al. (2017) conducted a comprehensive study on the influence of various parameters on the number of detected EMRIs, which has been adopted in subsequent works (e.g., Bonetti & Sesana 2020; Pozzoli et al. 2023). Their analysis showed that a positive SMBH mass function slope (see Eq. 36) results in a low detection rate, below a few tens of EMRIs per year.

When considering the SMBH mass function adopted here, with its negative slope, the key factor leading to the broad range in the predicted number of sources is the EMRI-to-plunge ratio. While Babak et al. (2017) treated it as a free parameter, in our model the EMRI-to-plunge ratio is fully determined by the dynamics and the sBH number fraction, f_{\bullet} . For a typical value of $f_{\bullet} \approx 10^{-3}$, we find roughly 2.5 plunges per EMRI (see Table 2), contrary to the commonly assumed values of $\approx 10 - 100$ (e.g., Alexander 2017; Babak et al. 2017). This difference arises from the stronger mass segregation in our model, which leads to a reduced number of plunges. Even for a mass fraction as large as $f_{\bullet} \approx 10^{-2}$,

our model predicts only about 20 more plunges than EMRIs.

Additionally, Babak et al. (2017) consider the effects of the SMBH spin, the $M_{\text{BH}} - \sigma_h$ relation, and cusp erosion. These factors typically introduce order unity changes in the expected number of sources and are not included in our analysis.

We note that the intrinsic EMRI rate per galaxy used by Babak et al. (2017) is based on the Fokker-Planck calculations of Amaro-Seoane & Preto (2011) for a strongly segregated cusp. Amaro-Seoane & Preto (2011) predict several hundreds EMRIs per Gyr, for a Milky Way-like galaxy, a value that is comparable to our result (Eq. 20). Furthermore, their scaling relation, $\Gamma_{\text{EMRI}} \propto M_{\text{BH}}^{-0.19}$, is similar to our analytical result: $\Gamma_{\text{EMRI}} \propto M_{\text{BH}}^{-0.25}$.

Overall, when comparing our estimated detection rates with those of Babak et al. (2017), Bonetti & Sesana (2020), and Pozzoli et al. (2023), we observe that our predictions consistently fall above their results for the fiducial model (M1) and below their results for the “optimistic” model (M12), despite the differences in model assumptions and calculation methods. This trend aligns with the fact that our model analytically finds a lower number of plunges per EMRI than the M1 model and a higher number than M12 model, highlighting the significant influence of this parameter (as previously noted by Babak et al. 2017). In our analysis, this is not a free parameter but calculated from the dynamics, as discussed in Section 3.

Last, our GWB characteristic strain scaling, $h_{c,\text{GWB}} \propto f^{-1.26}$, is steeper than the $h_{c,\text{GWB}} \propto f^{-1}$ obtained by Bonetti & Sesana (2020). Additionally, We estimate the GWB SNR (following Bonetti & Sesana 2020; Pozzoli et al. 2023), yielding $\text{SNR}_{\text{GWB}} \approx 1500$, which is also between the values calculated by Bonetti & Sesana (2020) for the M1 and M12 models. Note that Pozzoli et al. (2023) found that the detection rates and GWB SNR are lower by a factor of a few, compared to the results presented here and those from Babak et al. (2017) and Bonetti & Sesana (2020). For a detailed discussion, see Section V.a of Pozzoli et al. (2023).

It is worth noting that the GWB calculations in Bonetti & Sesana (2020) and Pozzoli et al. (2023) follow a different approach than the one applied here. They employ an iterative estimation of the GWB energy density (following Phinney 2001), including the summation of higher GW harmonics and the subtraction of resolvable sources. Additionally, beyond the different model assumptions discussed above, each of the cited works, including our own, adopted slightly different sensitivity curves for LISA and waveform models that also con-

tribute to the deviations in the results, if expressed in terms of SNR.

6. SUMMARY

In this work, we study the dynamics around SMBHs, focusing on the formation of EMRIs, driven by two-body scattering, and its implications for LISA observations. We combine the steady-state solution, due to two-body scattering, as derived by Linial & Sari (2022), with a GW-induced dissipation. This leads to a schematic division of the phase space into a scattering-dominated region and a GW-dominated one, as depicted in Fig. (1). Each region is further characterized by a broken-power-law distribution, as given in Eq. (15).

Using the above result, we estimate the formation rates of EMRIs and plunges, per SMBH, and the EMRI eccentricity distribution, which are qualitatively comparable to previous results in the literature (see Section 5), although derived from a different model for the steady-state distribution in NSCs.

However, our model differs from previous estimations in its prediction of the EMRI-to-plunge ratio; while it is usually assumed that plunges are more prevalent than EMRIs, our model predicts that if the sBH population is scarce, i.e, its number fraction $f_{\bullet} < f_{\bullet}^c \simeq 4.5 \times 10^{-4}$, the EMRI rate will exceed the plunge rate. For more massive sBHs, the critical number density, f_{\bullet}^c , is smaller and the EMRI-to-plunge ratio increases more rapidly, as evident in Fig. (3).

We further estimate the GWB induced by a cosmological population of EMRIs, which hampers the LISA sensitivity in the range 1 – 5 mHz, by up to a factor of ≈ 2 around 2.5 mHz. Accordingly, we estimate that during a 4 yr mission, LISA will detect approximately 2×10^3 resolvable sources, with SNR greater than $\text{SNR}|_{\text{th}} = 20$.

1 This research was partially supported by an ISF grant,
 2 an NSF/BSF grant, and an MOS grant. B.R. acknowl-
 3 edges support from the Milner Foundation. I.L. ac-
 4 knowledges support from a Rothschild Fellowship, The
 5 Gruber Foundation, and a Simons Investigator grant,
 6 827103. K.K. gratefully acknowledges support from the
 7 Israel Science Foundation (Individual Research grant
 8 2565/19).

APPENDIX

A. FORMATION RATES OF EMRIS & PLUNGES

The distribution of a population of sBHs with a given mass m_\bullet , i.e., the equivalent to Eq. (15), can be derived following the same steps described in Section (2), in a straightforward yet algebraically cumbersome manner. Here, we present explicitly the expressions for the formation rates of EMRIs and plunges. As in Section (3), we assume $R_{\text{GW}} \ll R_{\text{I}}, R_c \ll R_h$. To simplify the notation, we denote $\tilde{m}_\bullet = m_\bullet/m_\star$.

Considering the EMRI rate, from Eq. (20), we get

$$\Gamma_{\text{EMRI}} \simeq 1050 \tilde{m}_\bullet^{-3/5} \left(\frac{M_{\text{BH}}}{M_{\text{MW}}} \right)^{-1/4} \begin{cases} 1 & f_\bullet > f_\bullet^c \\ 75 (f_\bullet \tilde{m}_\bullet)^{4/5} \left[1 + \frac{4}{\tilde{m}_\bullet - 5} \left(1 - 0.013^{(5-\tilde{m}_\bullet)/4} (f_\bullet \tilde{m}_\bullet)^{\tilde{m}_\bullet/5-1} \right) \right] & f_\bullet < f_\bullet^c \end{cases} \quad (\text{A1})$$

The plunge rate, Eq. (21), is given by

$$\Gamma_{\text{Plunge}} \simeq 78216 \left(\frac{M_{\text{MW}}}{M_{\text{BH}}} \right)^{1/4} \begin{cases} f_\bullet^{4/5} \tilde{m}_\bullet^{1/5} \left[1 + \frac{4}{\tilde{m}_\bullet - 5} - 0.01 (f_\bullet \tilde{m}_\bullet)^{-4/5} \right] & f_\bullet > f_\bullet^c \\ 4 (f_\bullet \tilde{m}_\bullet)^{(\tilde{m}_\bullet - 1)/5} \frac{0.013^{(5-\tilde{m}_\bullet)/4}}{\tilde{m}_\bullet^{3/5} (\tilde{m}_\bullet - 5)} & f_\bullet < f_\bullet^c \end{cases} \quad (\text{A2})$$

Finally, using the above results, we get the EMRI-to-plunge ratio in the limiting cases:

$$\frac{\Gamma_{\text{EMRI}}}{\Gamma_{\text{Plunge}}} \simeq \begin{cases} 55 (\tilde{m}_\bullet - 1) 0.013^{\tilde{m}_\bullet/4} (f_\bullet \tilde{m}_\bullet)^{1-\tilde{m}_\bullet/5} & f_\bullet \ll f_\bullet^c \\ 0.01 \frac{\tilde{m}_\bullet - 5}{\tilde{m}_\bullet - 1} (f_\bullet \tilde{m}_\bullet)^{-4/5} & f_\bullet \gg f_\bullet^c \end{cases} \quad (\text{A3})$$

B. GW EMISSION FROM CIRCULAR ORBITS - GR CORRECTIONS

We estimate the GR strong-field correction to the GW emission under the adiabatic approximation (for further details, see [Apostolatos et al. 1993](#); [Hughes 2000](#); [Hughes et al. 2005](#)). Namely, we treat the sBH as a test particle that slowly descends from one circular geodesic, with radius R , to another. Thus, the radial velocity can be determined by the orbital-averaged power emitted in GWs, which we determine using the semianalytical method introduced by [Rom & Sari \(2022\)](#).

Under these assumptions, the GR correction introduces two modifications to the weak-field approximation ([Peters 1964](#)): (a) an increased radiated power near the ISCO, by roughly $\sim 15\%$; and (b) a shallower effective potential at the ISCO vicinity ([Misner et al. 1973](#)), which shortens the merger time ([Ori & Thorne 2000](#); [Buonanno & Damour 2000](#)).

Following [Finn & Thorne \(2000\)](#), we define the GR corrections relative to the weak-field approximation. Therefore, the GR corrections to the GWs' strain, h , and characteristic time for changing the orbital frequency, f/\dot{f} (Eq. 34), are given by

$$\varepsilon_h = \sqrt{\frac{\dot{E}_{\infty,2}}{\dot{E}|_Q}}, \quad (\text{B4})$$

$$\varepsilon_f = \frac{f/\dot{f}}{f/\dot{f}|_Q} = \frac{R/R_s - 3}{2(R/R_s - 3/2)(R/R_s - 1)} \frac{\dot{E}/E|_Q}{\dot{E}_\infty/E}, \quad (\text{B5})$$

where \dot{E}_∞ is the total power radiated to infinity, $\dot{E}_{\infty,2}$ is the power radiated to infinity in the quadrupole mode, and $\dot{E}|_Q = (m_\bullet/M)^2 (R_s/R)^5 / 5$ and $E|_Q = -GM_{\text{BH}} m_\bullet / (2R)$ are the weak-field estimates.

Combining the above results, the correction to the characteristic strain for evolving sources is

$$\begin{aligned} \varepsilon_{h_c} &= \varepsilon_h \sqrt{\varepsilon_f} = \left[\frac{R/R_s}{(R/R_s - 3/2)^3} \right]^{1/4} \sqrt{\left(\frac{R}{R_s} - 3 \right) \frac{\dot{E}_{\infty,2}}{\dot{E}_\infty}} \\ &\simeq \left(1 - \frac{\xi_f}{2} \right)^{-3/4} \sqrt{(1 - \xi_f) \left(1 - \frac{\alpha}{3} \xi_f \right)}, \end{aligned} \quad (\text{B6})$$

where $\xi_f = (f/f_{\text{ISCO}})^{2/3}$ and f_{ISCO} is twice the orbital frequency at the ISCO. Following Rom & Sari (2022), we approximate $\frac{\dot{E}_{\infty,2}}{\dot{E}_{\infty}} \simeq 1 - \alpha(R_s/R)$. Numerically, we find that for $\alpha = (4/5)^2$ our approximation agrees with the numerical result, with a relative error less than 0.5%.

Considering sources at the local Universe (Section 4.1), the effect of the GR corrections can be estimated as follows. For evolving sources, i.e., $f > f_s$, the contribution of the most massive SMBH, $M_{\text{BH}} = M_{\text{max}}$ is suppressed due to the reduced merger time near the ISCO (Eq. B5). This can be taken into account effectively by integrating up to a smaller maximal SMBH mass, $\Upsilon \times M_{\text{max}}$, where $\Upsilon \simeq \begin{cases} 0.5 & f_{\bullet}/f_{\bullet}^c \lesssim 0.6 \\ 0.65 \times \min\{1, (f_{\bullet}/f_{\bullet}^c)^{3/5}\} & f_{\bullet}/f_{\bullet}^c \gtrsim 0.6 \end{cases}$. Thus, the effective maximal SMBH mass corresponds to the SMBH for which the sBH orbits at $R \approx 5R_s$ or at $R = R_{\text{II}}$. The former is relevant for $f_{\bullet} \lesssim 0.6f_{\bullet}^c$, where $R_{\text{II}} \gtrsim 5R_s$, while the latter is valid at larger values of f_{\bullet} , such that $4R_s \leq R_{\text{II}} \lesssim 5R_s$. This modification translates to an effective parameter $\varepsilon \approx 0.82$ in Eq. (37).

On the other hand, for steady sources at low frequencies, $f < f_s$, the reduced merger time is relevant only at the immediate vicinity of the ISCO, as M_{max} is larger at low frequencies and therefore its impact is subdominant. In this case, we find that the effective GR correction is mild; the full numerical results are well captured by taking $\varepsilon = 0.93$. This can be attributed to the reduced emission power in the $m = 2$ mode, resulting in a slightly weaker strain, $\varepsilon \approx \varepsilon_h(R_{\text{ISCO}})$.

C. COSMOLOGICAL MODEL

We assume a standard flat Λ CDM model, where $\Omega_{\Lambda} = 0.68$, $\Omega_M = 0.32$, and $H_0 = 67 \text{ km s}^{-1}\text{Mpc}^{-1}$ are the dark energy density, matter density, and Hubble constant, respectively (Planck Collaboration et al. 2020).

The luminosity distance, $d_L(z)$, and the comoving volume, dV_c/dz , are given by

$$d_L(z) = (1+z) \frac{c}{H_0} \int_0^z \frac{d\tilde{z}}{\varrho(1+\tilde{z})} = \frac{c}{H_0} \eta(1+z), \quad (\text{C7})$$

$$\frac{dV_c}{dz} = 4\pi \left(\frac{c}{H_0}\right)^3 \frac{\left(\int_0^z \frac{d\tilde{z}}{\varrho(1+\tilde{z})}\right)^2}{\varrho(1+z)} = 4\pi \left(\frac{c}{H_0}\right)^3 \frac{[\eta(1+z)/(1+z)]^2}{\varrho(1+z)}, \quad (\text{C8})$$

where $\varrho(x) = \sqrt{\Omega_{\Lambda} + \Omega_M x^3}$, and

$$\eta(x) = \frac{x}{\sqrt{\Omega_{\Lambda}}} \left[x \tilde{F} \left(-\frac{\Omega_M}{\Omega_{\Lambda}} x^3 \right) - \tilde{F} \left(-\frac{\Omega_M}{\Omega_{\Lambda}} \right) \right], \quad (\text{C9})$$

with $\tilde{F}(x) = {}_2F_1(1/3, 1/2; 4/3; x)$, and ${}_2F_1(a, b; c; x)$ is the hypergeometric function.

REFERENCES

- Aharon, D., & Perets, H. B. 2016, ApJL, 830, L1, doi: [10.3847/2041-8205/830/1/L1](https://doi.org/10.3847/2041-8205/830/1/L1)
- Alexander, T. 2017, ARA&A, 55, 17, doi: [10.1146/annurev-astro-091916-055306](https://doi.org/10.1146/annurev-astro-091916-055306)
- Alexander, T., & Hopman, C. 2009, ApJ, 697, 1861, doi: [10.1088/0004-637X/697/2/1861](https://doi.org/10.1088/0004-637X/697/2/1861)
- Amaro-Seoane, P. 2018, Living Reviews in Relativity, 21, 4, doi: [10.1007/s41114-018-0013-8](https://doi.org/10.1007/s41114-018-0013-8)
- Amaro-Seoane, P., & Preto, M. 2011, Classical and Quantum Gravity, 28, 094017, doi: [10.1088/0264-9381/28/9/094017](https://doi.org/10.1088/0264-9381/28/9/094017)
- Amaro-Seoane, P., Andrews, J., Arca Sedda, M., et al. 2023, Living Reviews in Relativity, 26, 2, doi: [10.1007/s41114-022-00041-y](https://doi.org/10.1007/s41114-022-00041-y)
- Apostolatos, T., Kennefick, D., Ori, A., & Poisson, E. 1993, Phys. Rev. D, 47, 5376, doi: [10.1103/PhysRevD.47.5376](https://doi.org/10.1103/PhysRevD.47.5376)
- Arca Sedda, M., Naoz, S., & Kocsis, B. 2023, Universe, 9, 138, doi: [10.3390/universe9030138](https://doi.org/10.3390/universe9030138)
- Arcodia, R., et al. 2021, Nature, 592, 704, doi: [10.1038/s41586-021-03394-6](https://doi.org/10.1038/s41586-021-03394-6)
- Babak, S., Gair, J., Sesana, A., et al. 2017, Phys. Rev. D, 95, 103012, doi: [10.1103/PhysRevD.95.103012](https://doi.org/10.1103/PhysRevD.95.103012)
- Bahcall, J. N., & Wolf, R. A. 1976, ApJ, 209, 214, doi: [10.1086/154711](https://doi.org/10.1086/154711)
- . 1977, ApJ, 216, 883, doi: [10.1086/155534](https://doi.org/10.1086/155534)
- Balberg, S., & Yassur, G. 2023, The Astrophysical Journal, 952, 149, doi: [10.3847/1538-4357/acdd73](https://doi.org/10.3847/1538-4357/acdd73)

- Bar-Or, B., & Alexander, T. 2016, *ApJ*, 820, 129, doi: [10.3847/0004-637X/820/2/129](https://doi.org/10.3847/0004-637X/820/2/129)
- Bar-Or, B., Kupi, G., & Alexander, T. 2013, *ApJ*, 764, 52, doi: [10.1088/0004-637X/764/1/52](https://doi.org/10.1088/0004-637X/764/1/52)
- Barack, L., & Cutler, C. 2004, *PhRvD*, 70, 122002, doi: [10.1103/PhysRevD.70.122002](https://doi.org/10.1103/PhysRevD.70.122002)
- Binney, J., & Tremaine, S. 1987, *Galactic dynamics*
- Bonetti, M., & Sesana, A. 2020, *Phys. Rev. D*, 102, 103023, doi: [10.1103/PhysRevD.102.103023](https://doi.org/10.1103/PhysRevD.102.103023)
- Bortolas, E., & Mapelli, M. 2019, *Monthly Notices of the Royal Astronomical Society*, 485, 2125, doi: [10.1093/mnras/stz440](https://doi.org/10.1093/mnras/stz440)
- Broggi, L., Bortolas, E., Bonetti, M., Sesana, A., & Dotti, M. 2022, *Monthly Notices of the Royal Astronomical Society*, 514, 3270, doi: [10.1093/mnras/stac1453](https://doi.org/10.1093/mnras/stac1453)
- Buonanno, A., & Damour, T. 2000, *Phys. Rev. D*, 62, 064015, doi: [10.1103/PhysRevD.62.064015](https://doi.org/10.1103/PhysRevD.62.064015)
- Cornish, N., & Robson, T. 2017, *Journal of Physics: Conference Series*, 840, 012024, doi: [10.1088/1742-6596/840/1/012024](https://doi.org/10.1088/1742-6596/840/1/012024)
- Finn, L. S., & Thorne, K. S. 2000, *Phys. Rev. D*, 62, 124021, doi: [10.1103/PhysRevD.62.124021](https://doi.org/10.1103/PhysRevD.62.124021)
- Gair, J. R., Barack, L., Creighton, T., et al. 2004, *Classical and Quantum Gravity*, 21, S1595, doi: [10.1088/0264-9381/21/20/003](https://doi.org/10.1088/0264-9381/21/20/003)
- Gezari, S. 2021, *Annual Review of Astronomy and Astrophysics*, 59, 21, doi: [10.1146/annurev-astro-111720-030029](https://doi.org/10.1146/annurev-astro-111720-030029)
- Ghez, A. M., Salim, S., Weinberg, N. N., et al. 2008, *ApJ*, 689, 1044, doi: [10.1086/592738](https://doi.org/10.1086/592738)
- Gillessen, S., Eisenhauer, F., Trippe, S., et al. 2009, *ApJ*, 692, 1075, doi: [10.1088/0004-637X/692/2/1075](https://doi.org/10.1088/0004-637X/692/2/1075)
- Hills, J. G. 1988, *Nature*, 331, 687, doi: [10.1038/331687a0](https://doi.org/10.1038/331687a0)
- Hils, D., & Bender, P. L. 1995, *ApJL*, 445, L7, doi: [10.1086/187876](https://doi.org/10.1086/187876)
- Hopman, C. 2009, *Classical and Quantum Gravity*, 26, 094028, doi: [10.1088/0264-9381/26/9/094028](https://doi.org/10.1088/0264-9381/26/9/094028)
- Hopman, C., & Alexander, T. 2005, *The Astrophysical Journal*, 629, 362, doi: [10.1086/431475](https://doi.org/10.1086/431475)
- . 2006, *The Astrophysical Journal*, 645, L133, doi: [10.1086/506273](https://doi.org/10.1086/506273)
- Hughes, S. A. 2000, *PhRvD*, 61, 084004, doi: [10.1103/PhysRevD.61.084004](https://doi.org/10.1103/PhysRevD.61.084004)
- . 2002, *MNRAS*, 331, 805, doi: [10.1046/j.1365-8711.2002.05247.x](https://doi.org/10.1046/j.1365-8711.2002.05247.x)
- Hughes, S. A., Drasco, S., Flanagan, E. E., & Franklin, J. 2005, *Phys. Rev. Lett.*, 94, 221101, doi: [10.1103/PhysRevLett.94.221101](https://doi.org/10.1103/PhysRevLett.94.221101)
- Ivanov, P. B. 2002, *MNRAS*, 336, 373, doi: [10.1046/j.1365-8711.2002.05733.x](https://doi.org/10.1046/j.1365-8711.2002.05733.x)
- Kaur, K., Rom, B., & Sari, R. 2024, arXiv e-prints, arXiv:2406.07627. <https://arxiv.org/abs/2406.07627>
- Keshet, U., Hopman, C., & Alexander, T. 2009, *ApJL*, 698, L64, doi: [10.1088/0004-637X/698/1/L64](https://doi.org/10.1088/0004-637X/698/1/L64)
- Kormendy, J., & Ho, L. C. 2013, *Annual Review of Astronomy and Astrophysics*, 51, 511, doi: [10.1146/annurev-astro-082708-101811](https://doi.org/10.1146/annurev-astro-082708-101811)
- Lightman, A. P., & Shapiro, S. L. 1977, *ApJ*, 211, 244, doi: [10.1086/154925](https://doi.org/10.1086/154925)
- Linial, I., & Sari, R. 2022, *ApJ*, 940, 101, doi: [10.3847/1538-4357/ac9bfd](https://doi.org/10.3847/1538-4357/ac9bfd)
- . 2023, *ApJ*, 945, 86, doi: [10.3847/1538-4357/acbd3d](https://doi.org/10.3847/1538-4357/acbd3d)
- Mapelli, M. 2021, in *Handbook of Gravitational Wave Astronomy*, 16, doi: [10.1007/978-981-15-4702-7_16-1](https://doi.org/10.1007/978-981-15-4702-7_16-1)
- Mapelli, M., Ripamonti, E., Vecchio, A., Graham, A. W., & Gualandris, A. 2012, *A&A*, 542, A102, doi: [10.1051/0004-6361/201118444](https://doi.org/10.1051/0004-6361/201118444)
- Merritt, D. 2004, in *Coevolution of Black Holes and Galaxies*, ed. L. C. Ho, 263, doi: [10.48550/arXiv.astro-ph/0301257](https://doi.org/10.48550/arXiv.astro-ph/0301257)
- Merritt, D. 2015, *ApJ*, 814, 57, doi: [10.1088/0004-637X/814/1/57](https://doi.org/10.1088/0004-637X/814/1/57)
- Merritt, D., Alexander, T., Mikkola, S., & Will, C. M. 2010, *PhRvD*, 81, 062002, doi: [10.1103/PhysRevD.81.062002](https://doi.org/10.1103/PhysRevD.81.062002)
- Miniutti, G., Saxton, R. D., Giustini, M., et al. 2019, *Nature*, 573, 381, doi: [10.1038/s41586-019-1556-x](https://doi.org/10.1038/s41586-019-1556-x)
- Misner, C. W., Thorne, K. S., & Wheeler, J. A. 1973, *Gravitation* (San Francisco: W. H. Freeman), 636–670
- Naoz, S., & Haiman, Z. 2023, *ApJL*, 955, L27, doi: [10.3847/2041-8213/acf8c9](https://doi.org/10.3847/2041-8213/acf8c9)
- Nelemans, G., Yungelson, L. R., & Portegies Zwart, S. F. 2001, *A&A*, 375, 890, doi: [10.1051/0004-6361:20010683](https://doi.org/10.1051/0004-6361:20010683)
- Netzer, H. 2015, *Annual Review of Astronomy and Astrophysics*, 53, 365, doi: [10.1146/annurev-astro-082214-122302](https://doi.org/10.1146/annurev-astro-082214-122302)
- Nissanke, S., Vallisneri, M., Nelemans, G., & Prince, T. A. 2012, *ApJ*, 758, 131, doi: [10.1088/0004-637X/758/2/131](https://doi.org/10.1088/0004-637X/758/2/131)
- Ori, A., & Thorne, K. S. 2000, *Phys. Rev. D*, 62, 124022, doi: [10.1103/PhysRevD.62.124022](https://doi.org/10.1103/PhysRevD.62.124022)
- Peters, P. C. 1964, *Physical Review*, 136, 1224, doi: [10.1103/PhysRev.136.B1224](https://doi.org/10.1103/PhysRev.136.B1224)
- Peters, P. C., & Mathews, J. 1963, *Phys. Rev.*, 131, 435, doi: [10.1103/PhysRev.131.435](https://doi.org/10.1103/PhysRev.131.435)
- Phinney, E. S. 2001, arXiv e-prints, astro, doi: [10.48550/arXiv.astro-ph/0108028](https://doi.org/10.48550/arXiv.astro-ph/0108028)
- Planck Collaboration, Aghanim, N., Akrami, Y., et al. 2020, *A&A*, 641, A6, doi: [10.1051/0004-6361/201833910](https://doi.org/10.1051/0004-6361/201833910)
- Pozzoli, F., Babak, S., Sesana, A., Bonetti, M., & Karnesis, N. 2023, *PhRvD*, 108, 103039, doi: [10.1103/PhysRevD.108.103039](https://doi.org/10.1103/PhysRevD.108.103039)

- Qunbar, I., & Stone, N. C. 2023, arXiv e-prints, arXiv:2304.13062, doi: [10.48550/arXiv.2304.13062](https://doi.org/10.48550/arXiv.2304.13062)
- Rees, M. J. 1988, *Nature*, 333, 523, doi: [10.1038/333523a0](https://doi.org/10.1038/333523a0)
- Robson, T., Cornish, N. J., & Liu, C. 2019, *Classical and Quantum Gravity*, 36, 105011, doi: [10.1088/1361-6382/ab1101](https://doi.org/10.1088/1361-6382/ab1101)
- Rom, B., Linial, I., & Sari, R. 2023, *The Astrophysical Journal*, 951, 14, doi: [10.3847/1538-4357/acd54f](https://doi.org/10.3847/1538-4357/acd54f)
- Rom, B., & Sari, R. 2022, *Phys. Rev. D*, 106, 104040, doi: [10.1103/PhysRevD.106.104040](https://doi.org/10.1103/PhysRevD.106.104040)
- Rose, S. C., Naoz, S., Sari, R., & Linial, I. 2023, *The Astrophysical Journal*, 955, 30, doi: [10.3847/1538-4357/acee75](https://doi.org/10.3847/1538-4357/acee75)
- Ruiter, A. J., Belczynski, K., Benacquista, M., Larson, S. L., & Williams, G. 2010, *The Astrophysical Journal*, 717, 1006, doi: [10.1088/0004-637X/717/2/1006](https://doi.org/10.1088/0004-637X/717/2/1006)
- Sari, R., & Fragione, G. 2019, *ApJ*, 885, 24, doi: [10.3847/1538-4357/ab43df](https://doi.org/10.3847/1538-4357/ab43df)
- Schmidt, M. 1963, *Nature*, 197, 1040, doi: [10.1038/1971040a0](https://doi.org/10.1038/1971040a0)
- Sigurdsson, S., & Rees, M. J. 1997, *MNRAS*, 284, 318, doi: [10.1093/mnras/284.2.318](https://doi.org/10.1093/mnras/284.2.318)
- Timpano, S. E., Rubbo, L. J., & Cornish, N. J. 2006, *PhRvD*, 73, 122001, doi: [10.1103/PhysRevD.73.122001](https://doi.org/10.1103/PhysRevD.73.122001)
- Vasiliev, E., & Merritt, D. 2013, *ApJ*, 774, 87, doi: [10.1088/0004-637X/774/1/87](https://doi.org/10.1088/0004-637X/774/1/87)
- Vázquez-Aceves, V., Zwick, L., Bortolas, E., et al. 2022, *MNRAS*, 510, 2379, doi: [10.1093/mnras/stab3485](https://doi.org/10.1093/mnras/stab3485)
- Zwick, L., Capelo, P. R., Bortolas, E., et al. 2021, *MNRAS*, 506, 1007, doi: [10.1093/mnras/stab1818](https://doi.org/10.1093/mnras/stab1818)